JOURNAL OF AIRCRAFT
Vol. 43, No. 2, March–April 2006

Response of Damaged and Undamaged Tailored Extension-Shear-Coupled Composite Panels

Donald J. Baker*
NASA Langley Research Center, Hampton, Virginia 23681

The results of an analytical and experimental investigation of the response of composite I-stiffener panels with extension-shear coupling are presented. This tailored concept, when used in the panel cover skins of a tiltrotor aircraft wing, has the potential for increasing the aeroelastic stability margins and improving the aircraft productivity. The extension-shear coupling is achieved by using unbalanced ±45-deg plies in the skin. Experimental and STAGS analysis results are compared for eight I-stiffener panel specimens. The results indicate that the tailored concept would be feasible to use in the wing skin of a tiltrotor aircraft. Evaluation of specimens impacted at an energy level of 500 in.-lb indicate a minimal loss in stiffness and less than 30% loss in strength. Evaluation of specimens with severed center stiffener and adjacent skin indicated a strength loss in excess of 60%.

Introduction

ONE of the principal design challenges for the high-speed tiltrotor transport aircraft is achieving acceptable proprotor aeroelastic stability margins, which can restrict the operating airspeed of the tiltrotor aircraft in the high-speed airplane mode. The primary mechanism responsible for the proprotor stability problems is discussed by Popelka et al.[1] and will be briefly reviewed here. Historically, the most critical modes affecting the proprotor stability are the symmetric-wing beamwise bending mode (SWB) and the symmetric-wing chordwise bending mode (SWC). For these modes, the rotor can create destabilizing in-plane hub forces, which can overcome the structural and aerodynamic damping of the wing at high speed and can cause instability. The in-plane shear forces are generated by the rotor in response to the pylon perturbation pitch angle and pitch rate. The wing SWB mode, SWC mode, and symmetric-wing torsion mode dictate the pylon pitch rate and pitch angle. Proprotor stability can be influenced by changing the frequency placement of the wing modes and by modifying the mode shapes to alter the pylon dynamic response and reduce the destabilizing in-plane hub forces.

Minimizing the pylon pitch motion in the fundamental wing modes can affect the proprotor stability. Minimizing the pylon pitch component reduces the rotor destabilizing forces and increases the stability boundary as shown in Fig. 1. In a typical tiltrotor wing design, the rotor pylon pitches up as the wing bends upward in the SWB mode. For a conventional composite wing design with structurally balanced skin laminates, the wing provides no structural pitch/bending coupling to resist the nose-up pitch caused by pylon mass offsets. Unbalanced composite skins, on the other hand, can create nose-down structural twist as the wing bends upward to offset the pitch-up tendency from the pylon mass offsets. The net effect is reduced pitch/bending coupling and improved stability. The preceding discussion applies to the SWB mode only.

The effects of structural tailoring can be simply shown by considering the cantilever boxbeam shown in Fig. 2a. The direction of the −45-deg plies are shown on the figure. The forward and aft spar web is a balanced ±45-deg laminate. The upward bending from the pylon produces a compression load in the upper skin and a tension load in the lower skin as shown in Figs. 2a and 2b. The compression load in the upper skin produces a deflection in the forward direction. The tension load in the lower skin produces a deflection in aft direction. These deflections in the skins combine to produce a couple that results in a nose-down pitch as shown in Fig. 2c.

The feasibility of a composite tailored wing for a high-speed civil tiltrotor transport aircraft has been addressed by Popelka et al.,[2] using current analytical methods to design a tailored composite wing for a tiltrotor transport aircraft. Parametric studies show that the overall stability gains from composite tailoring can be limited because of conflicting structural design requirements imposed by the two critical modes of instability, SWB and SWC, and the necessity to balance the stability boundaries for both modes. The SWC mode stability can be improved by increasing the chordwise bending stiffness of the wing. The final tailored wing configuration was a three-stringer configuration with a 70/30 blend ratio of −45-deg/+45-deg plies for the skin laminate along with stringer cap and spar cap tailoring to improve the SWC mode.

A $\frac{1}{5}$-scale wing model was designed to have the same elastic characteristics as the full-scale tailored wing and was tested in a semispan aeroelastic model to demonstrate that composites techniques can be used to improve proprotor stability.[3] A direct comparison between the baseline and tailored wing stability boundaries indicates an increase over baseline of approximately 30 kn in the scaled model or 58 kn in the full-scale design. For a full-scale design, the 58-kn increase in the stability boundary represents a significant improvement.

The objective of the present study is to assess the detailed structural response of tailored panels with and without damage. Specifically, this research addresses: 1) development of a test method for testing coupled specimens and 2) demonstration of the coupled response of the full-scale wing panel subcomponents with and without impact and discrete source damage. The analytical and experimental results of the study are presented and compared to illustrate the predictive capability for stiffened, anisotropic panels.

Test Specimens

The panels to be evaluated were designed by Bell Helicopter, Textron, using the results of the study by Popelka et al.[2] A cross section of the stiffener and skin is shown in Fig. 3b. The skin is 21 plies increasing to 47 plies under the I-stiffener using Grade 190 IM6-3501-6 carbon-epoxy tape material. The skin orientation is $[45/90/-45_3/45/-45_3/45/\bar{0}]_s$, where 67% of the 45-deg plies are oriented at the negative angle. The ply orientation for the reinforced area under the stiffener is $[45/90/-45_3/45/a/0_3/a/-45_2/a/0_4/a/-45/45/0/45/-45/a/0_4/a/-45_2/a/0_3/a/45/-45_3/90/45/a/45^f/-45^f/a]$, where "a" identifies a 0.008-in.-thick layer of FM300 adhesive. The I-stiffener is made from back-to-back C-channels, which have the following lay up: $[-45/90_2/45/0_4/-45/0_4/45/0_4/45/0_2]$. The cap of the I-stiffener

Presented as Paper 2003-1461 at the 43rd SDM, Norfolk, VA, 7 April 2003–9 April 2003; received 8 February 2005; revision received 22 April 2005; accepted for publication 9 June 2005.

*Aerospace Engineer, Mechanics and Durability Branch, Vehicle Technology Directorate—ARL.

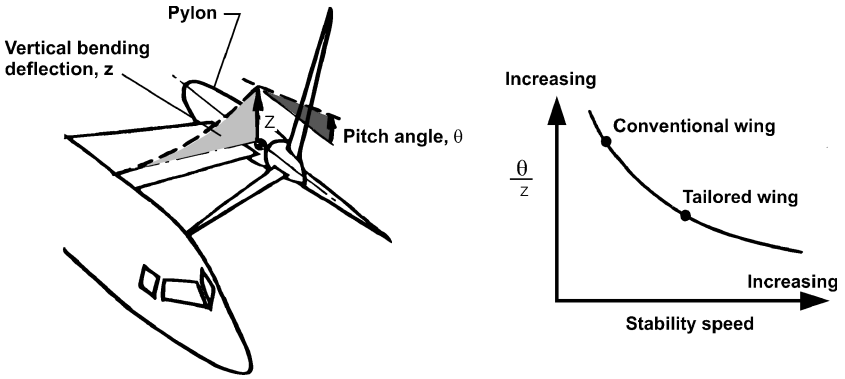

Fig. 1 Influence of structural tailoring on wing aeroelastic stability.

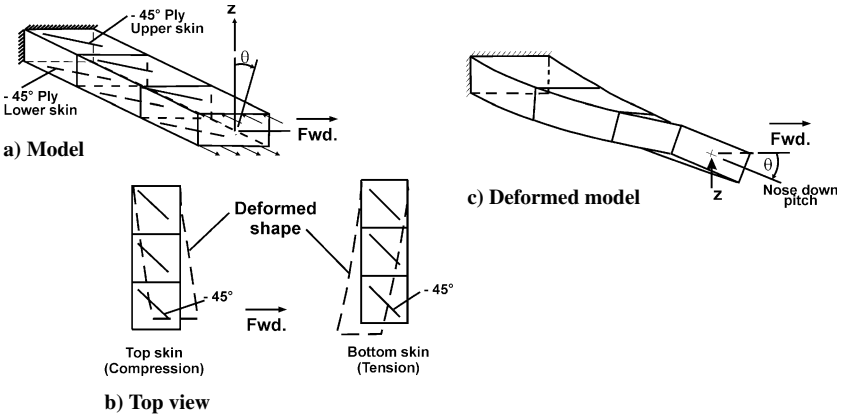

Fig. 2 Simple box-beam model.

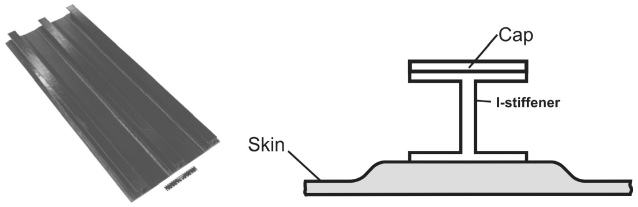

a) As-fabricated panel **b) Typical panel cross section at stiffener**

Fig. 3 Specimen configuration.

has a lay up of $[0_2/-45/0_4/-45/0_4/45/0_4/-45/90_2/45]$. The material for the stiffener and cap is Grade 95 IM6-3501-6 carbon-epoxy material. The stringer spacing is 7.5 in., which gives an overall panel width of approximately 19 in.

Four 4-ft-long panels, as shown in Fig. 3a, were manufactured at two different times. These panels were cut into 23-in.-long test specimens, potted and ground flat and parallel. These test specimens will be identified as TP-1 through TP-8 in the remainder of the paper. Specimens TP-1, TP-2, and TP-6 were tested in the as-fabricated (undamaged) condition. A slot was cut through the center stringer and adjacent skin on specimens TP-4, TP-5, and TP-7. Specimens TP-3 and TP-8 were subjected to low-speed impact at the thickness transition at the center stringer. Previous testing[4] on nontailored panels with the same design indicated that the thickness transition area is a critical point and 500 in.-lb of impact energy produced barely visible impact damage.

Test Procedures

All specimen tests were performed at room temperature, with no environmental conditioning. The specimens were placed between the platens of a 600-kip or 1200-kip hydraulic test machine and loaded in compression. The load rate varied depending on the specimen condition. For example, the undamaged specimens were loaded at 20 kips/min, whereas the specimens with the central slot were loaded at 5 kips/min.

Impact testing was performed using a dropped weight impactor, utilizing a 25-lb weight with a 1.0-in.-diam spherical impactor. The energy level was 500 in.-lb and was intended to produce barely visible impact damage.

All specimens were instrumentated with strain gages with the number of gages varying with specimen condition. Specimen strain gage instrumentation patterns are shown later in the paper. Out-of-plane displacement were measured using linear variable displacement transducers (LVDT) at selected locations. The load, strain, out-of-plane, and head displacements were recorded with a computer-controlled data-acquisition system for each test. In addition to the strain gages and displacement transducers used during the test, a three-dimensional image correlation technique[5] was also used. This full-field-displacement measurement technique utilizes a camera-based stereovision system. This is a nonintrusive system because the only part of the measurement system that comes into contact with the test specimen is a spackle pattern that is applied to the surface of the test specimen to establish the specimen displacement tracking points. The spackle pattern that is applied to the surface of the test specimen can be a thin contact film with a black spackle pattern printed on the film or black paint dots on a white background. Images of the changing pattern on the test specimen surface are recorded at user-specified time intervals to monitor the displacement field.

Testing a tailored panel with extension-shear coupling presents some unique challenges. It is necessary to maintain a uniform applied displacement along the end of the panel as the panel changes shape because of the extension-shear coupling, from a rectangle to a parallelogram as shown in Fig. 4. Maintaining a uniform displacement and allowing the end of the test specimen to move in plane required a test fixture as shown in Fig. 5. The fixture shown in Fig. 5 is attached to the end of the test specimen. The rollers shown allow the test specimen to move in plane while the axial displacement is applied to the top plate with a test machine.

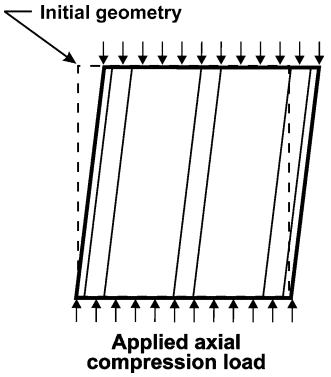

Fig. 4 Effect of extension-shear coupling on panel response.

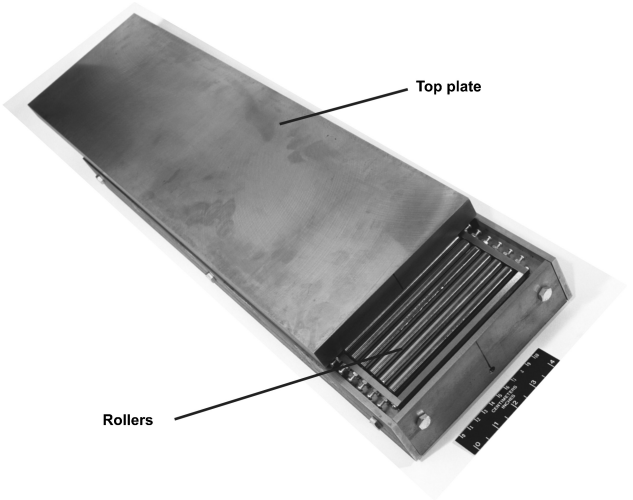

Fig. 5 Test fixture for panels with coupled in-plane response.

Results and Discussion

Because there are three types of specimens—1) undamaged, 2) with cut center stringer and adjacent skin, and 3) impact damaged, results for each type will be presented individually. Each section will include a brief specimen description, comparison of analysis and test results, and failure mode description. Finite element analysis of the panels was conducted using STAGS nonlinear analysis code[6] to determine test specimen response. STAGS (STructural-Analysis of General Shells) is a general-purpose finite element analysis code for the analysis of shell structures of arbitrary shape and complexity.

Undamaged Specimens

The STAGS finite element model of the undamaged specimen is shown in Fig. 6. This model contained 12,420 of STAGS four-node quad elements (element 410 in STAGS library) and 12,649 nodes. Analysis results for an undamaged specimen are presented in Figs. 7 and 8 for an applied load P in the y direction. The fringe pattern shown in Fig. 7 is for the w displacement field (out of plane) in the test specimen. The analysis predicted localized out-of-plane displacements at each end in the skin as shown by the teardrop-shaped contours. Because of skin displacements, the center stiffener is predicted to deflect out-of-plane, but there is no indication of the edge stiffeners deflecting out of plane. The fringe patterns shown in Fig. 8 are for the u-displacement field (normal to the stiffener direction) in the test specimen. The effect of the extension-shear coupling is indicated by the skewed pattern of these fringes. The predicted u displacement in the panel is approximately 17% of the v displacement. Only the u displacement at the panel centerline is considered when computing the in-plane displacement to eliminate the Poisson effect on the specimen edges.

The linear buckling analysis of the undamaged specimen predicted the first mode buckling at 31.12 kips/in.

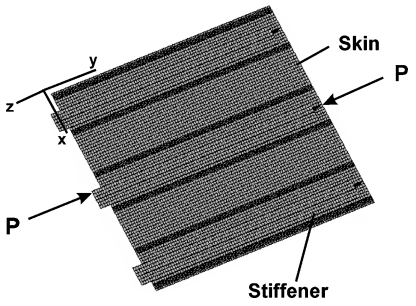

Fig. 6 Finite element model of undamaged test specimen.

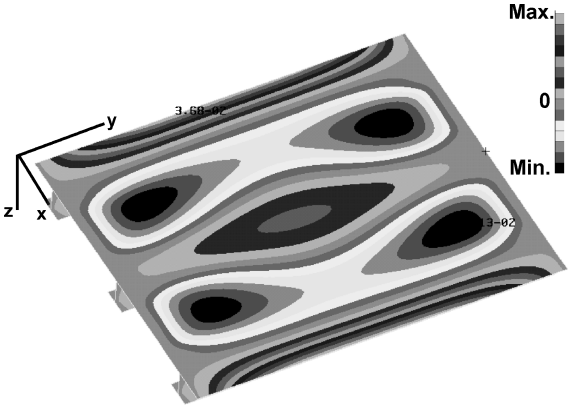

Fig. 7 Typical analytical out-of-plane displacement contours.

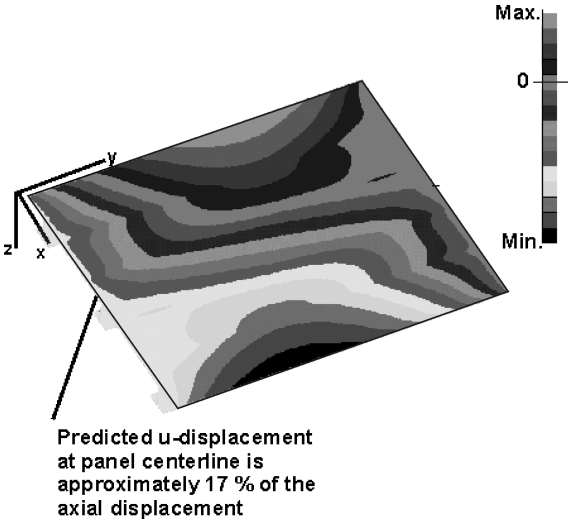

Fig. 8 Typical analytical in-plane displacement contours.

Three undamaged specimens, TP-1, TP-2, and TP-6, have been tested. A photograph of TP-1 is shown in Fig. 9, along with the strain gages. Specimens TP-1 and TP-2 had a total of 36 strain gages each, located along the specimen midlength and quarter-point length as shown in Fig. 9. The other undamaged specimen, TP-6, was instrumented with 18 strain gages along the quarter-point length.

The undamaged specimens were loaded in compression at the rate of 20 kips/min until failure. The failure loads are shown in Table 1 for each specimen. The average failure load was 20.43 kips/in. One specimen of a similar design with a balanced ±45-deg skin stacking sequence has been tested with a failure load of 22.7 kips/in.[4] The tailoring reduces the failure strength by approximately 10%. A plot of the specimen axial end shortening (solid lines) and transverse in-plane displacement (dashed lines) as a function of load is shown in Fig. 10. The slope of the axial displacement curve is

considered a measure of the specimen stiffness. The stiffness of each specimen is shown in column 3 of Table 1. The average specimen stiffness of 146.17 kips/in./in. is approximately 5% lower than the computed stiffness of 153.89 kips/in./in. The transverse in-plane (dashed line) plot for each specimen indicates the amount of in-plane displacement that resulted from the coupling. The amount of in-plane displacement as a fraction of the axial displacement, for each specimen, is shown in column 4 of Table 1. The computed in-plane displacement is 0.17 times the axial displacement. The difference between analysis and test results for specimens TP-1 and TP-2 could be because they were produced in different batches compared to specimen TP-6.

Table 1 Undamaged specimen loads and stiffnesses

Specimen number	Failure load, kips/in.	Stiffness, kips/in./in.	P[a]
TP-1	21.64	144.42	0.25
TP-2	20.59	146.21	0.25
TP-6	19.07	147.89	0.17

[a]In-plane displacement is P times the axial displacement.

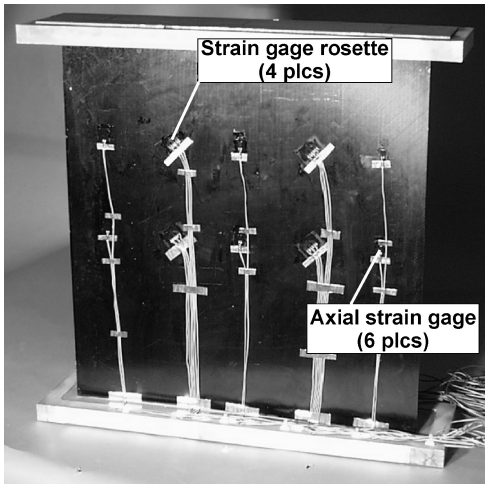

Fig. 9 Test specimen, TP-1.

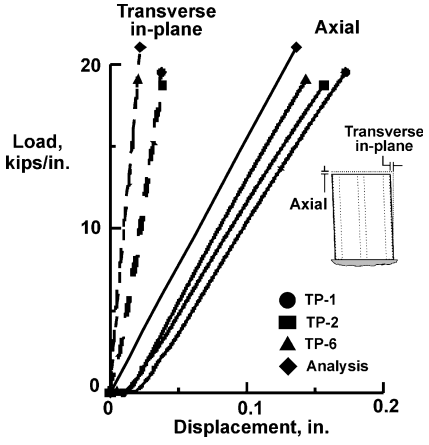

Fig. 10 Axial and in-plane displacement as a function of applied load.

Strain gage results from gages located at the quarter-point of specimen TP-1 length are shown in Fig. 11. The back-to-back gages (Fig. 11a) indicate bending in the center stiffener and no bending in the outer stiffeners. As shown in Fig. 11a, the stiffeners do not carry a uniform strain across the specimen width with the strains at failure varying from 0.002 in./in. in the center stiffener to 0.006 in./in. in the stiffener denoted by the triangle symbols. Results from the skin bays indicate some bending and a tension strain of approximately 0.002 in./in. These strain gages are located in areas where the analysis predicted an out-of-plane deflection. The shear strains in the skin denoted by the triangle symbol indicate less than 0.0005 strain, while the other skin bay indicated approximately 0.002 strain. There are very small shear-strain gradients through the thickness of the skin panel. The axial strain gages at the center of specimen TP-1 were all near 0.006 in/in. at failure and indicated a slight nonlinearity as a function of load. The strain gage results indicated some bending in the center I-stiffener at the specimen centerline as predicted by analysis. The shear strain in the skin bays at specimen centerline had up to 0.002 shear-strain gradient through the skin thickness. These observations suggest that the strain state in the panels is very complex.

In addition to the strain gages and displacement transducers used during the testing, a three-dimensional image correlation system, described earlier, was also used. Some of the results that have been obtained from the image correlation system on specimen TP-1 are illustrated in Fig. 12. As shown in Fig. 12, the image area covered approximately top one-half of the specimen surface area. The first image taken in any test determines the profile (or flatness) of the specimen at no load. Specimen TP-1 profile is shown in Fig. 12a and indicates the specimen surface profile varies from a theoretical plane by +0.010- to −0.005-in. Each contour line represents a constant distance from a theoretical plane. The initial imperfections are tracked to access the reproducibility of these tailored panels. U-displacement contours are presented in Fig. 12b. These contours indicate that the in-plane displacement is approximately 16% of the axial displacement. The effect of the specimen Poisson's ratio, which is nearly unity for the skin laminate, can be observed along the edges of the specimen. The v-displacement contours shown in Fig. 12c indicate a nearly uniform axial loading of the panel. The w-displacement contours are shown in Fig. 12d. The skin between the I-stiffeners and located between the quarter-point and the specimen end deflect up to 0.06-in. out of plane. This out-of-plane displacement magnitude compares well with the analysis results. The skin deflections are maximum in the bay on the left side of the figure. The analysis (see Fig. 7) also predicts the skin deflection on one side of the center stiffener will have a greater magnitude.

The profile of specimen TP-6 is shown in Fig. 13. The image area of this specimen is larger than the area shown in Fig. 12 and extends approximately 3 in. past the centerline. The out of flatness of this specimen varies from −0.005 to +0.06-in. from a theoretical plane.

The strain on the surface viewed with the image correlation system can be computed from the displacement measurements. The ε_{yy} strain computed from the displacements on specimen TP-6 skin

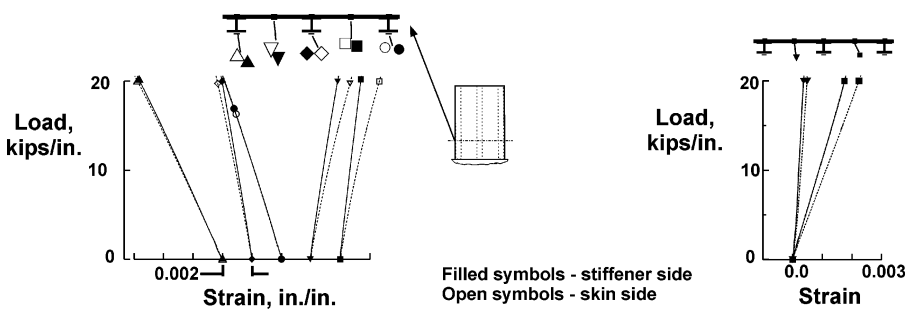

a) Axial strain **b) Shear strain**

Fig. 11 Load-strain results for specimen TP-1 along a line at the specimen quarter-length.

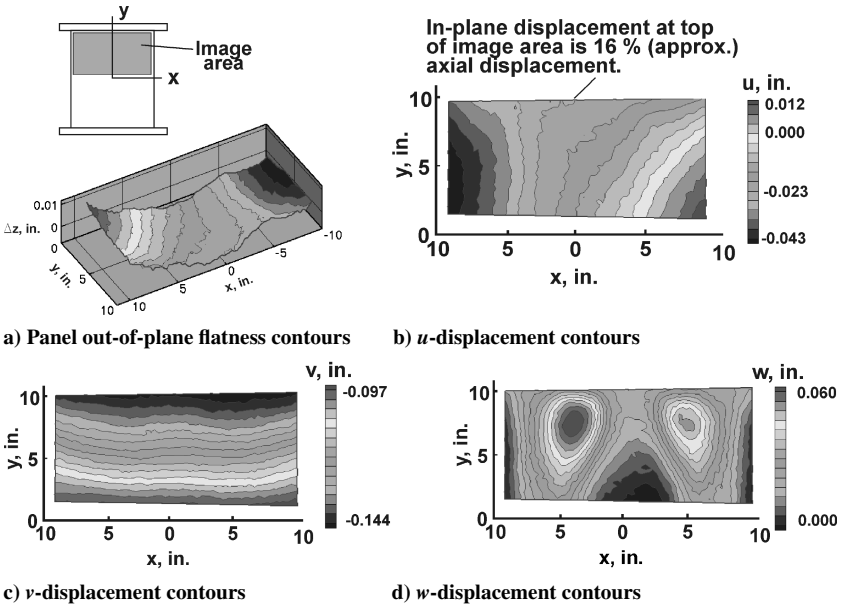

Panel TP1 - Image taken at load = 21.6 kips/in.

Fig. 12 Results obtained from the image correlation analysis on specimen TP-1.

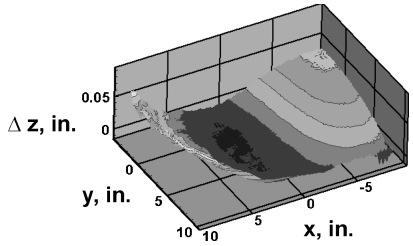

Fig. 13 Profile of specimen TP-6.

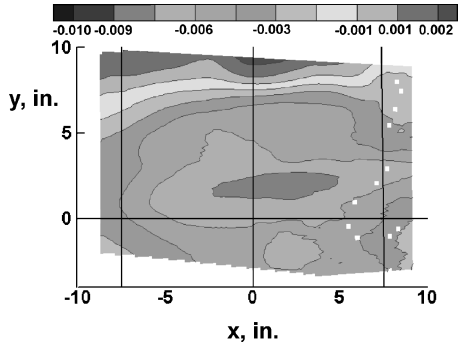

Fig. 14 Skin surface strains (ε_{yy}) for specimen TP-6 at 18.67-kips/in. load.

surface is shown in Fig. 14. The strain on the skin surface shown in Fig. 14 varies from +0.001 in./in. (near top edge) to −0.007 in./in. for a load of 18.87 kips/in. with the maximum compressive strain located approximately 2 in. above the specimen centerline. The predicted surface strain for a load of 18.95 lb/in. is shown in Fig. 15. The predicted strain in the central area of the specimen is 0.0061 in./in. and compares well with the strain determined from the image correlation system. The analysis results indicate strain concentration at each end in the skin. This effect is also indicated in Fig. 14, along the top edge.

Photographs of failed specimen TP-6 are shown in Fig. 16. The stiffeners failed along the bondline with the skin. The failure has both adhesive and cohesive characteristics. The skin also failed in one corner as shown in Fig. 16. Specimens TP-1 and TP-2 also failed by stringer separation similar to specimen TP-6.

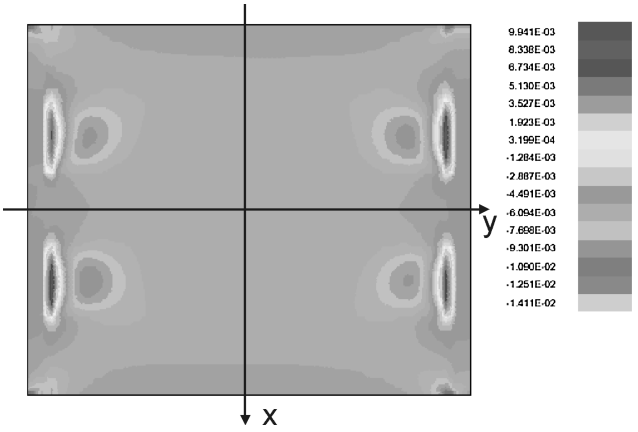

Fig. 15 Predicted strain on TP-6 skin surface.

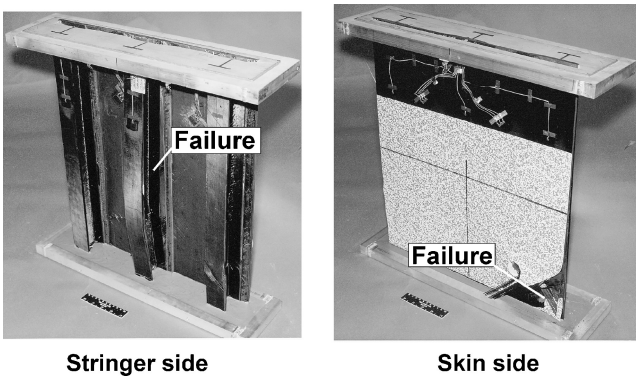

Fig. 16 Failed specimen TP-6.

Damaged Specimens

Horizontal Cut

The specimens, TP-4 and TP-7, were damaged by cutting the center stringer and adjacent skin as shown in Fig. 17. The slot extends between the center of each skin panel and is 0.38-in. wide at the center of the specimen tapering to 0.18-in. wide at the ends with a tip radius of 0.09-in.

The STAGS finite element model of the damaged specimen with a horizontal slot is shown in Fig. 18. This model contained 12,771

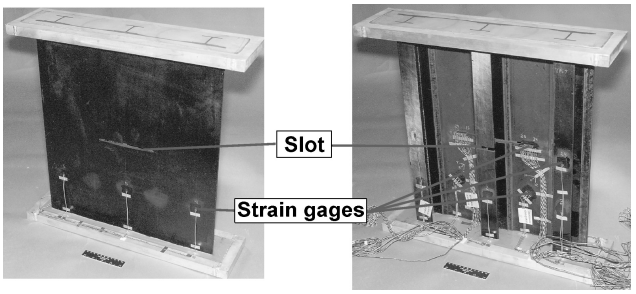

Fig. 17 Specimen with horizontal slot.

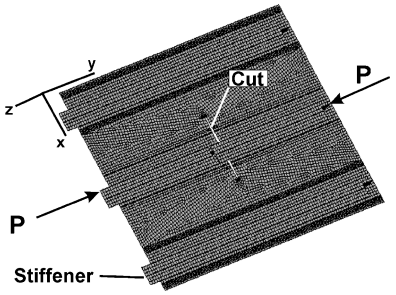

Fig. 18 Finite element model of specimen with horizontal slot.

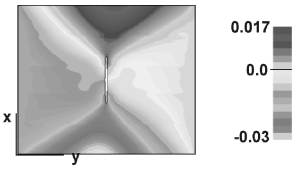

a) u-displacement

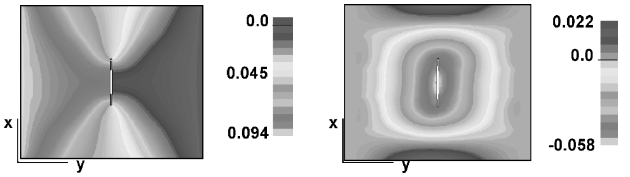

b) v-displacement c) w-displacement

Fig. 19 Predicted displacements for specimen with horizontal slot.

quad elements and 12,494 nodes. Predicted displacement results are shown in Fig. 19 for a specimen with a horizontal slot. These contours (Fig. 19a) do not have the skewed pattern shown in Fig. 7 for the undamaged specimen. The severing of the center stiffener and adjacent skin minimizes the extension-shear coupling in the specimen. The contours shown in Fig. 19b indicate the load redistribution around the central slot. The large triangular area to the right of the slot in Fig. 19b indicates no axial displacement. Figure 19c indicates an out-of-plane bulge caused by severing the central stiffener.

The linear buckling analysis of the damaged specimen predicted the first mode to be 14.73 kips/in.

A photograph of the damaged specimens, TP-4 and TP-7, is shown in Fig. 17. These specimens contain 34 strain gages that are located at the quarter-length of the specimen and adjacent to the end of the slot.

The damaged specimens were loaded in compression at the rate of 5 kips/min until failure. The failure loads are shown in Table 2 for each specimen. The average failure load for the two specimens is 7.65 kips/in. The residual strength of the specimens with a horizontal slot is 37% of the residual strength of the undamaged specimens. A plot of the specimen axial end shortening and transverse in-plane displacement as a function of load is shown in Fig. 20. The stiffness of each specimen is shown in column 3 of Table 2. The average specimen stiffness of 100.2 kips/in./in. and is approximately 12% below the computed stiffness of 114 kips/in./in. The transverse in-plane displacements are also shown in Fig. 20 as dashed lines. Specimen

Table 2 Failure load and stiffness for specimens with a horizontal slot

Specimen number	Failure load, kips/in.	Stiffness kips/in./in.
TP-4	7.80	103.1
TP-7	7.51	97.3

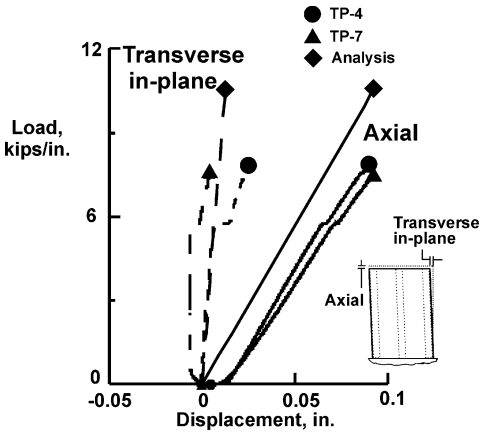

Fig. 20 Axial and transverse in-plane displacements as a function of applied load.

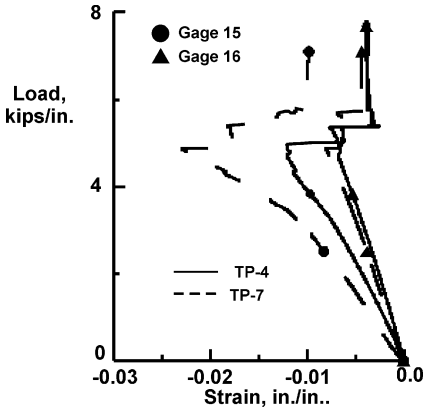

Fig. 21 Results from gages at end of slot.

TP-4 transverse in-plane displacement is the same as the analysis predictions until a failure at approximately 5.5 kips/in. The analysis predicted the in-plane displacement to be 14% of axial displacement. Specimen TP-7 does not show any in-plane displacement until the earlier failure noted.

Strain gage results from two strain gages adjacent to the slot are shown in Fig. 21. Strain gage 15 is at the slot end, and gage 16 is located 0.1-in. from gage 15. As shown in Fig. 21, both specimens had an initial failure at approximately 5.5 kips/in. Although the strain in gage 15 on specimen TP-7 is twice the strain in gage 15 on specimen TP-4, the strains at gage 16 are nearly equal in both specimens.

The profiles of both specimens determined by the image correlation system are shown in Figs. 22 and 23. An option available to the image correlation system is to add a second system of cameras, etc., to be able to focus on a local area of the specimen. For these specimens a local, 4- $\times$ 4-in., area was defined at one end of the slot. This local image area was painted white with black painted dots while the global image area was covered with a 0.004-in. thick vinyl with the black pattern printed on it. This local area can be observed in Figs. 22 and 23 as a square area at the slot end depressed from the surrounding area. Most of specimen TP-4 varies $\pm$0.010 in. from the theoretical plane. A local area near one edge varies up to 0.05 from the plane. The profile of specimen TP-7 (Fig. 23) varies from $-$0.005 to $+$0.060 in. from a theoretical plane.

The w-displacement field and ε_{yy} strain field shown in Fig. 24 are the first images after any failure is observed in TP-7, which was at a

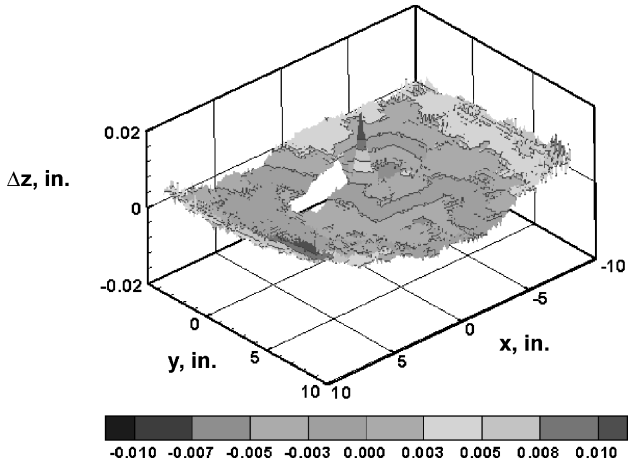

Fig. 22 Profile of specimen TP-4.

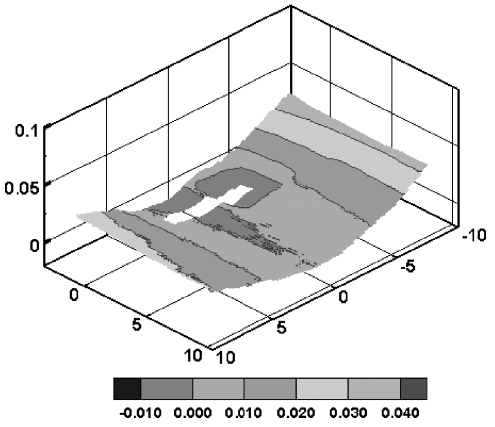

Fig. 23 Profile of specimen TP-7.

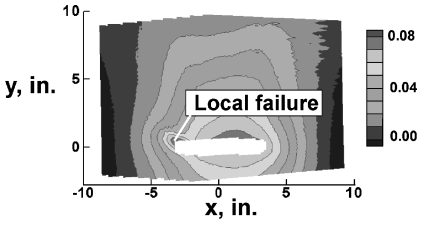

a) *w* displacement, in.

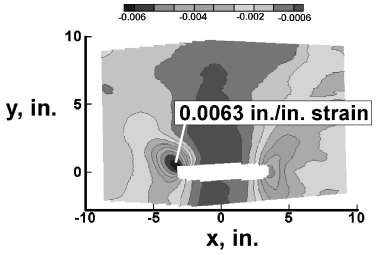

b) ε_{yy} strain

Fig. 24 Specimen TP-7 displacement and strain fields at 5.73-kips/in. compression load.

load of 5.73 kips/in. The local failure starts at the left upper corner of the slot as shown in Fig. 24a. The strain at the point of failure is 0.0063 in./in. as shown in Fig. 24b and compares well with adjacent gages shown in Fig. 21. Two images later at a load of 5.82-kips/in. failure starts at the right side of the slot as shown in Fig. 25. The local failures progress up and to the left and down and to the right until total specimen failure at 7.51 kips/in. Specimen TP-4 failed in a similar manner.

Both specimens, TP-4 and TP-7, failed in a similar manner. A photograph of the stringer side of specimen TP-4 is shown in Fig. 26.

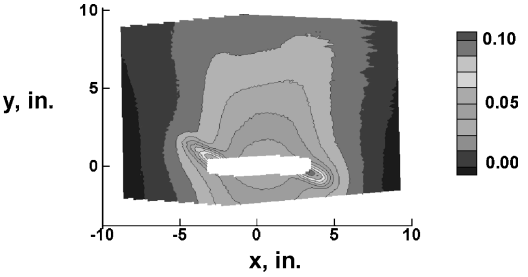

Fig. 25 Out-of-plane displacement contours for specimen TP-7 at 5.82-kips/in. compression load.

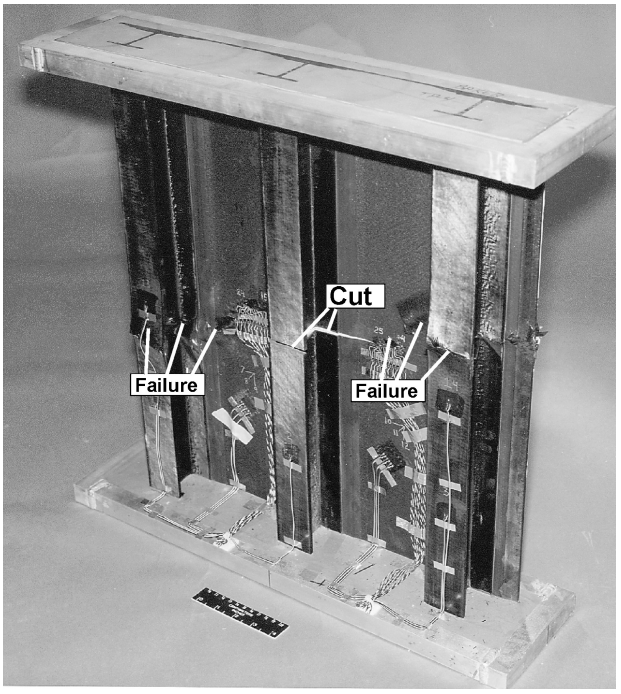

Fig. 26 Photograph of failed in specimen TP-4.

As indicated in the figure, the failure progressed from the end of the cut up or down across the skin. Once the failure intersected the stiffener, the failure path turned perpendicular to the stiffener and continued to the edge of the panel.

Inclined Cut

Specimen TP-5 also had the center stiffener cut similar to specimens TP-4 and TP-7 except the cut was rotated 15 deg from the horizontal as shown in Fig. 27. The STAGS finite element model of the specimen with the inclined cut is shown in Fig. 28. This model contains 12,702 quad elements and 12,429 nodes. Predicted displacement results are shown in Fig. 29 for a specimen with an inclined slot. These contours do not show a predominantly skewed pattern, but the analysis does predict the transverse in-plane displacement to be 16.8% of the axial displacement. This predicted transverse in-plane displacement is approximately 3% higher than the prediction for specimens with a horizontal slot. The displacement contours in Fig. 29b indicate the load redistribution around the central slot. The large triangular area to the right of the slot in Fig. 29b indicates no axial displacements. The predicted out-of-plane displacements are shown in Fig. 29c. These displacements are different than the displacement for a specimen with a horizontal slot. The top end of the slot as shown in Fig. 29c deflects in the positive direction (into the paper) while the bottom end deflects in the negative direction. This is entirely different than the bulge predicted for the specimen with a horizontal slot.

The linear buckling analysis of the specimen with an inclined slot predicted the first buckling mode to be at a load of 14.1 kips/in.

Specimen TP-5, shown in Fig. 27, was loaded in compression at the rate of 5 kips/min until failure occurred at 7.54 kips/in. The

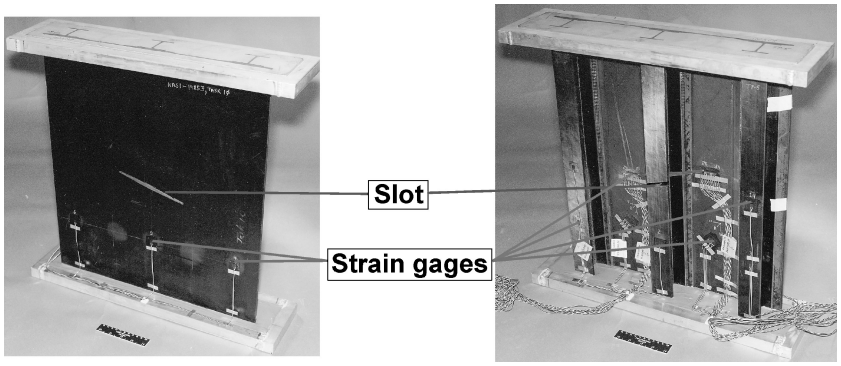

Fig. 27 Specimen TP-5 with inclined slot.

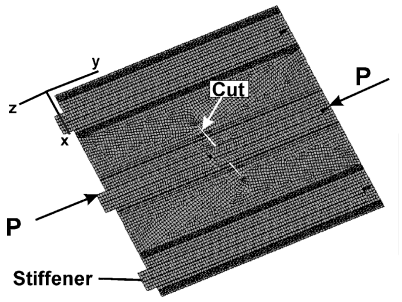

Fig. 28 Finite element model of specimen with inclined slot.

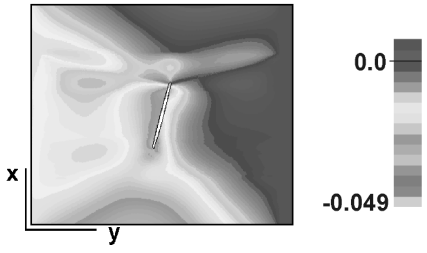

a) *u* displacement

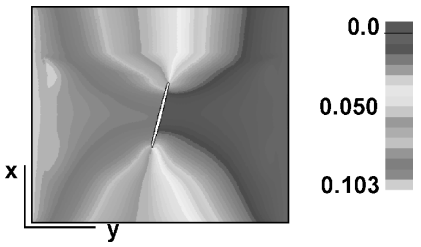

b) *v* displacement

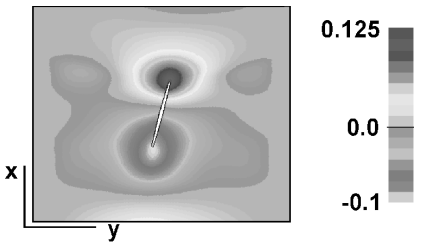

c) *w* displacement

Fig. 29 Predicted displacements for specimen with a inclined slot.

residual strength of specimen TP-5 is 37% of the residual strength of the undamaged specimens. A plot of the axial shortening and in-plane displacement as a function of load is shown in Fig. 30. The specimen stiffness of 96.1 kips/in./in. is approximately 13% below the computed stiffness of 110.1 kips/in./in. The in-plane displacement for specimen TP-5 is linear until an apparent failure occurred at a load of 6.3 kips/in.

The w-displacement field and ε_{yy} strain field for specimen TP-5 shown in Fig. 31 are for a load of 6.32 kips/in., which are just

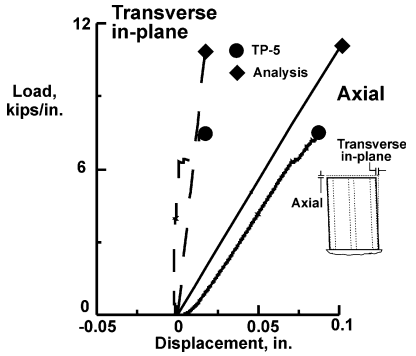

Fig. 30 Axial and transverse in-plane displacement as a function of applied load for specimen TP-5.

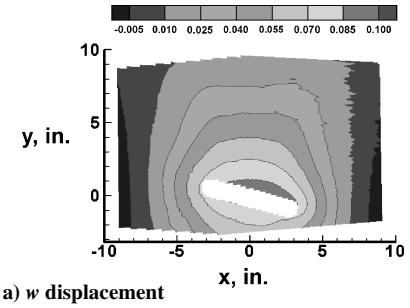

a) *w* displacement

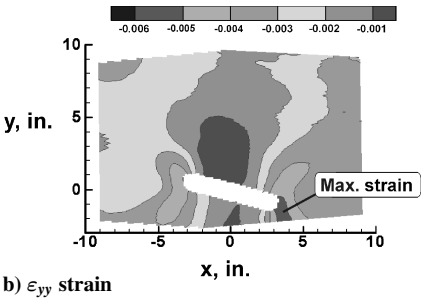

b) ε_{yy} strain

Fig. 31 Experimental displacement and strain fields for specimen TP-5 for $N_y = 6.32$ kips/in.

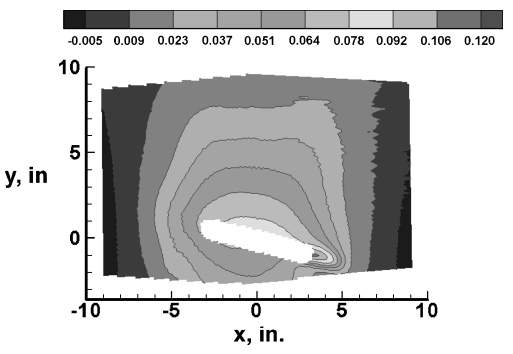

Fig. 32 *W*-displacement field on specimen TP-5 at $N_y = 6.33$ kips/in.

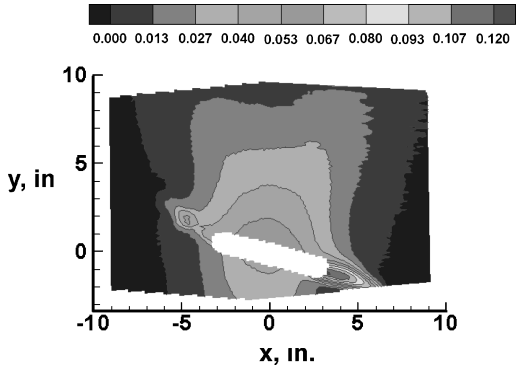

Fig. 33 Experimental *w*-displacement field on specimen TP-5 for $N_y = 7.45$ kips/in.

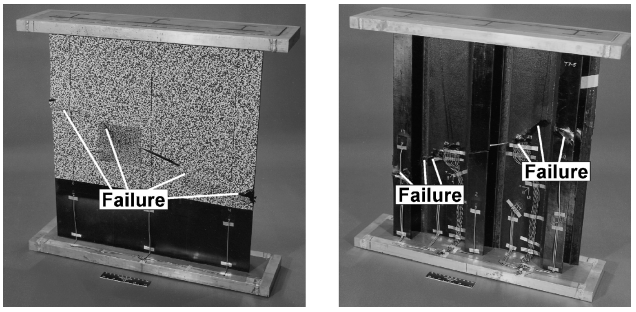

Fig. 34 Failed specimen TP-5.

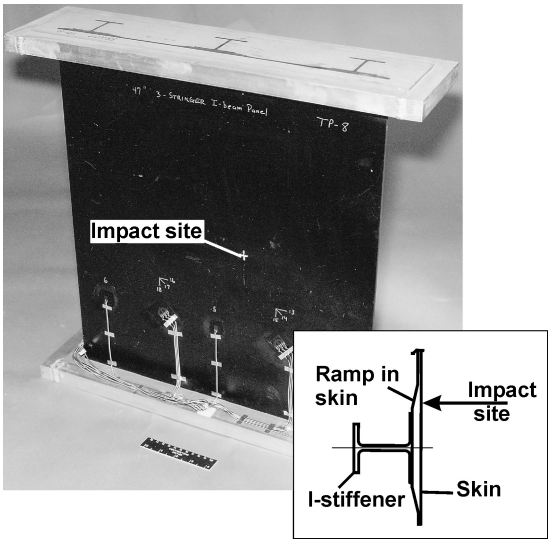

Fig. 35 Specimen TP-8.

prior to the failure initiation. Figure 31a indicates that the out-of-plane displacement is in the same direction on both sides of the centerline. This displacement field does not match the analysis result, which predicts the skin to deflect in opposite directions on each side of the centerline. The darker area at the right end of the slot in Fig. 31b indicates the maximum strain in the image area, and the strain is higher than on the left side of the slot. The displacement field shown in Fig. 32 is at a load of 6.33 kips/in. and indicates starting of delamination at the right side of the slot, where the highest strain was indicated in Fig. 31b. The displacement field at a load of 7.45 kips/in., which is near failure, is shown in Fig. 33. The failure can be seen emanating from both ends of the slot and going upward on the left side and downward on the right side.

Failed specimen TP-5 is shown in Fig. 34. The failure started at each end of the slot and progressed up or down until the stiffener location and then turned closer to a direction perpendicular to the stiffener and progressed to the specimen edge.

Impact Damage

Specimens TP-3 and TP-8 were impacted at an energy level of 500 in.-lb on the skin side opposite the ramp between the skin and the built-in skin reinforcement under the I-stiffeners as shown in Fig. 35. The impact was at the specimen midlength approximately 2 in. from the specimen centerline. The impact produced barely visible impact damage with dent depth of 0.008 in. (TP-3) and 0.005 in. (TP-8).

The profile of specimen TP-8, is shown in Fig. 36, which covers approximately 60% of the specimen area. The specimen flatness varies from -0.015 to $+0.045$ in. from a theoretical plane. As indicated earlier, the correlation system has an option to view a local area inside a global area. The local area around the impact site on specimen TP-8 is also shown in Fig. 36 as a three-dimensional view. The depth of the surface dent is 0.005 in., which is identical in magnitude to the value determined using a depth micrometer. The specimen curves from the center to the edges by up to 0.045 in.

The impacted specimens, TP-3 and TP-8, were loaded in compression at the rate of 20 kips/min until failure. The failure loads are

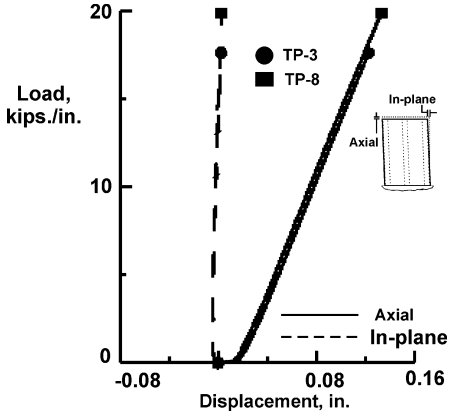

Fig. 37 Axial and in-plane displacement as a function of load for impacted specimens.

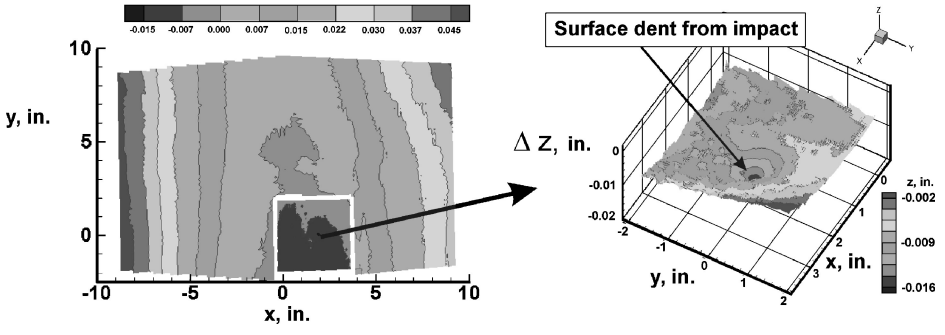

Fig. 36 Profile of specimen TP-8.

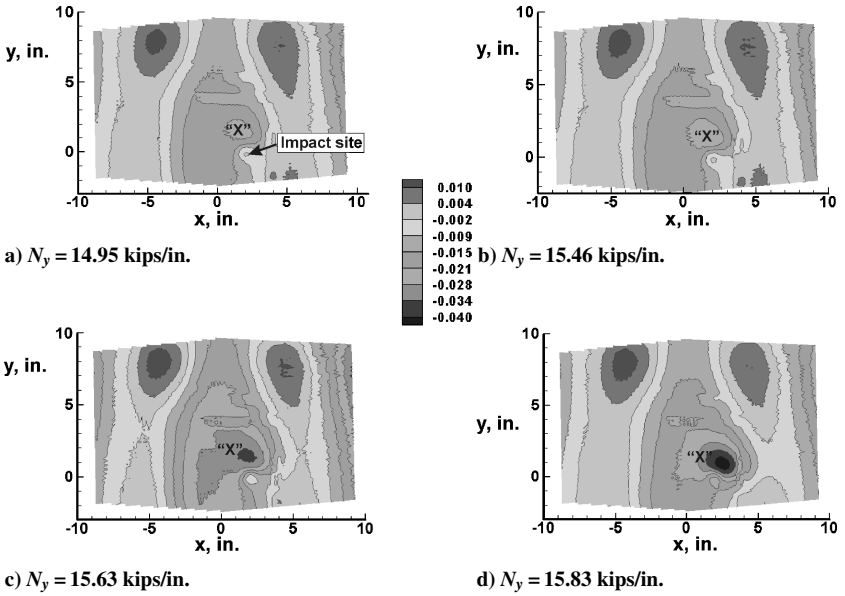

Fig. 38 Progression of increasing out-of-plane displacements in the vicinity of the impact damage site.

Table 3 Failure load and stiffness for impacted specimens

Specimen number	Failure load, kips/in.	Stiffness, kips/in./in.
TP-3	14.07	136.21
TP-8	15.87	136.3

shown in Table 3 for each specimen. The average failure load was 14.97 kips/in. The average residual strength of the impacted specimens is 73% of the undamaged strength. A plot of the impacted specimen axial shortening as a function of applied load is shown in Fig. 37.

The stiffness of each specimen is shown in column 3 of Table 3. The average stiffness of the impacted specimens is 136.26 kips/in./in., which is 93% of the average stiffness of the undamaged specimens. LVDT results indicated very little displacement in the transverse in-plane direction. A series of contour plots from the image correlation system shown in Fig. 38 indicate delamination growth. The area shown in Fig. 38a and identified by "X" is adjacent to the impact area and appeared at a much lower load than indicated as an area setting above the adjacent area but did not indicate any significant growth. Comparison of Figs. 38a and 38b indicate the area has a significant growth in size for approximately a 0.5 kip/in. increase in load. An increase in load of 0.17 kip/in. increases the size of the delamination areas and the magnitude of total deformation in the surrounding area as indicated by the increase in the contour level of the dark area as shown in Fig. 38c. The last image taken before failure is shown in Fig. 38d, which again indicates a significant growth in the delamination size for 0.2 kip/in. increase in load. The skin out-of-plane displacements (teardrop-shaped areas) show very little change when the delamination increases in size.

The in-plane contours for specimen TP-8 at $N_y = 15.63$ kips/in. are shown in Fig. 39. The in-plane contours shown in Fig. 39 indicate some in-plane displacement contrary to the minimum displacement indicated by the LVDTs.

The failed impacted specimen TP-8 is shown in Fig. 40. On the skin damaged as a result of impact, the failure progressed straight across the skin and stiffener to the edge of the panel on one side. Along the other side failure progressed at approximately a 45-deg angle to the stiffener, crossed the stiffener, and moved to the specimen edge at approximately a right angle to the stiffener.

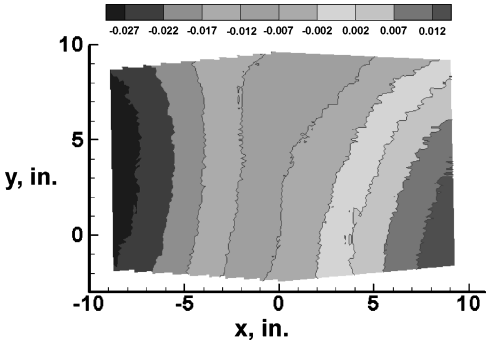

Fig. 39 In-plane contours for specimen TP-8 for N_y = 15.63 kips/in.

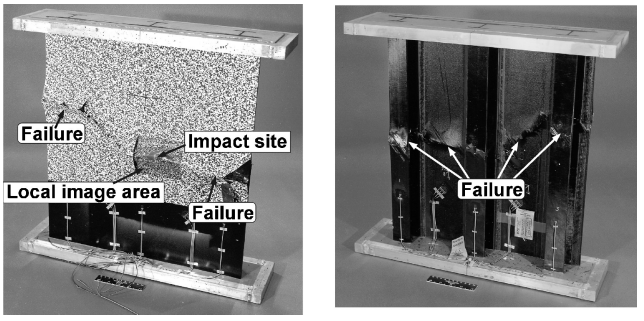

Fig. 40 Failed specimen TP-8, N_y = 15.87 kips/in.

Conclusions

A method has been developed for compression testing of tailored composite specimens with in-plane shear coupling that allows the specimen to deform from a rectangle to a parallelogram. The response of eight tailored composite panels have been studied using this test method.

Three specimen configurations have been evaluated: 1) undamaged (as-fabricated), 2) center stringer and adjacent skin severed, and 3) barely visible impact damage on the skin at a critical location.

The three undamaged tailored composite specimens have been tested, and the average strength was 90% of a specimen tested previously that had the same geometry with a balanced ±45-deg skin. The surface profiles of the panels indicated most of the panel was within 0.010 in. with some variations at the edge to as much as

0.06 in. The average specimen axial stiffness is within 5% of the computed stiffness from the STAGS analysis. The in-plane coupling is shown to induce transverse in-plane displacement magnitudes that are 17 to 25% of the axial displacements.

The specimens with the center stiffener and adjacent skin severed had a residual strength of 37% of the undamaged specimens. Accounting for the net section loss caused by introducing the cut, this amounts to a strength reduction of approximately 40 percent. The initiation of a local failure on the surface, viewed with the image correlation system was determined for the slotted specimens. The failures progressed upward or downward from the end of the slots depending on the local anisotropy of the material.

Specimens impacted for barely visible impact damage exhibited an average residual strength that was 73% of the undamaged specimen strength. The delamination growth with increasing load was tracked using the image correlation system. The impact damage pattern is also skewed because of anisotropy and results in an unsymmetrical growth to failure.

References

[1]Popelka, D., Sheffler, M., and Bilger, J., "Correlation of Test and Analysis for the 1/5th Scale V-22 Aeroelastic Model," *Journal of the American Helicopter Society*, Vol. 42, No. 2, 1997, pp. 126–136.

[2]Popelka, D., Lindsay, D., Parham, T., Jr., Berry, V., and Baker, D., "Results of an Aeroelastic Tailoring Study for a Composite Tiltrotor Wing," American Helicopter Society, Alexandria, VA, May 1995.

[3]Corso, L. M., Popelka, D. A., and Nixon, M. W., "Design, Analysis, and Test of a Composite Tailored Tiltrotor Wing," American Helicopter Society, April 1997.

[4]Rousseau, C. Q., Baker, D. J., and Hethcock, J. D., "Parametric Study of Three-Stringer Compression-After-Impact Strength," *Composite Structures: Theory and Practice*, ASTM, Conshohocken, PA, Oct. 2000, pp. 72–104.

[5]Helm, J. D., McNeil, S. R., and Sutton, M. A., "Improved Three-Dimensional Image Correlation for Surface Displacement Measurements," *Optical Engineering*, Vol. 35, No. 7, 1996, pp. 1911–1920.

[6]Brogan, F. A., Rankin, C. C., and Cabiness, H. D., "STAGS Users Manual," Lockheed Palto Alto Research Lab., Report LNSC P032594, June 2000.